

APPENDICES

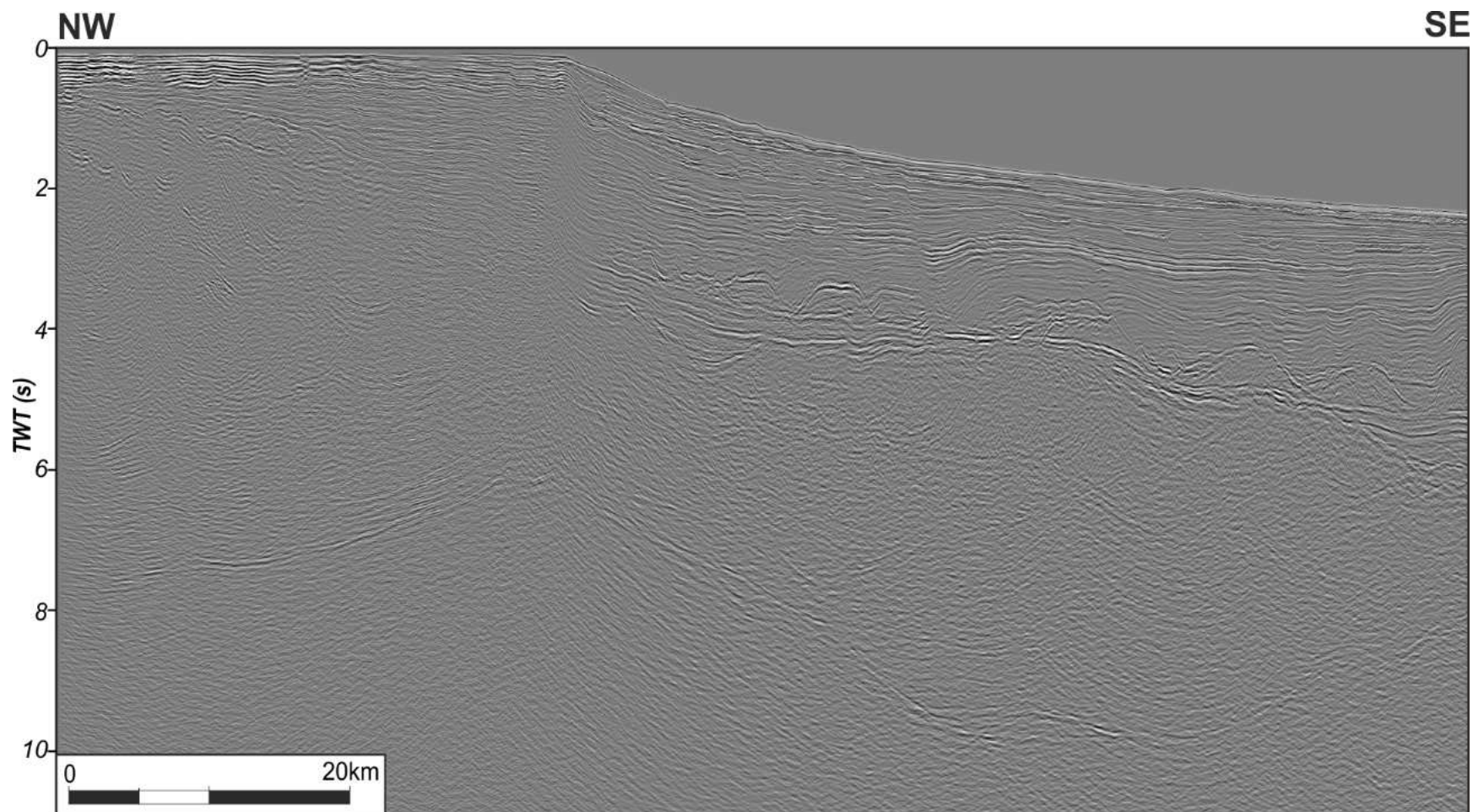


Figure A1: Uninterpreted seismic section of Figure 4b.

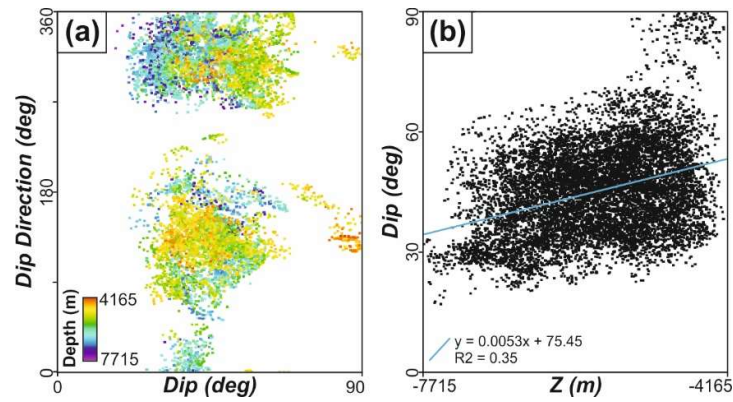


Figure A2: Cross plots showing the distribution of the nodes of the fault planes. a) dip vs dip direction, where the colours represent the depth. Notice the two main clusters defining a geometric conjugate set of NE-SW striking faults, a secondary pair of clusters defining a N-S-striking geometric conjugate set of faults. b) depth vs dip angle with the respective linear regression. The trend line shows a clearly negative correlation between depth and dip angle.

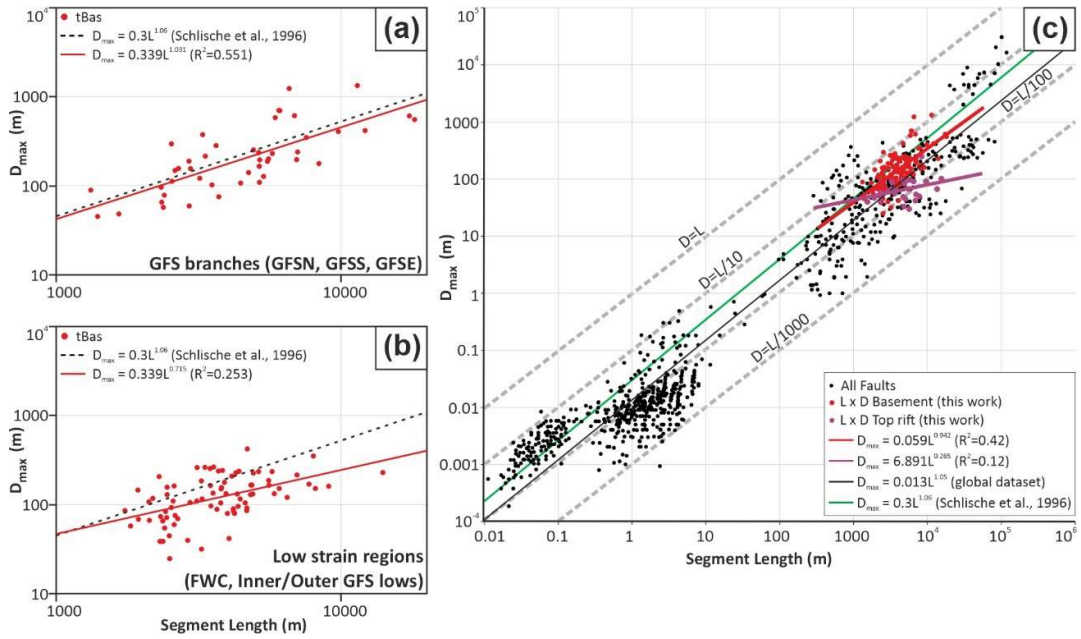


Figure A3: Length-maximum displacement (L-Dmax) data at tBas horizon plotted in log-log space for (a) fault segments within the GFS branches (b) fault segments elsewhere (FWC, Inner and Outer GFS Lows). (c) L-Dmax data and trend lines at tBas horizon (red) and at tRift (purple) in comparison with the global dataset for normal faults (Schlische et al., 1996; Kim & Sanderson, 2005 and references therein, Schlagenhauf et al., 2008; Schultz et al., 2008 and references therein, Morley, 2017). L-Dmax log-log trend line for tRift horizon (in purple) is also superposed to the global dataset graph. The comparison between 'a' and 'b' suggests that faults are mature and underdisplaced or immature, respectively (c.f.(McLeod et al., 2000). Similar behavior is observed in 'c' for tBas and tRift trend lines, which could be explained by the constant-length model for normal fault growth (Cowie, 1998) recently updated to a hybrid growth pattern (Rotevatn et al., 2019). Still in 'c', the LxDmax points for tBas fit well in the trend line of (Schlische et al., 1996). Such adjustment is even better for the faults within the GFS branches (a).

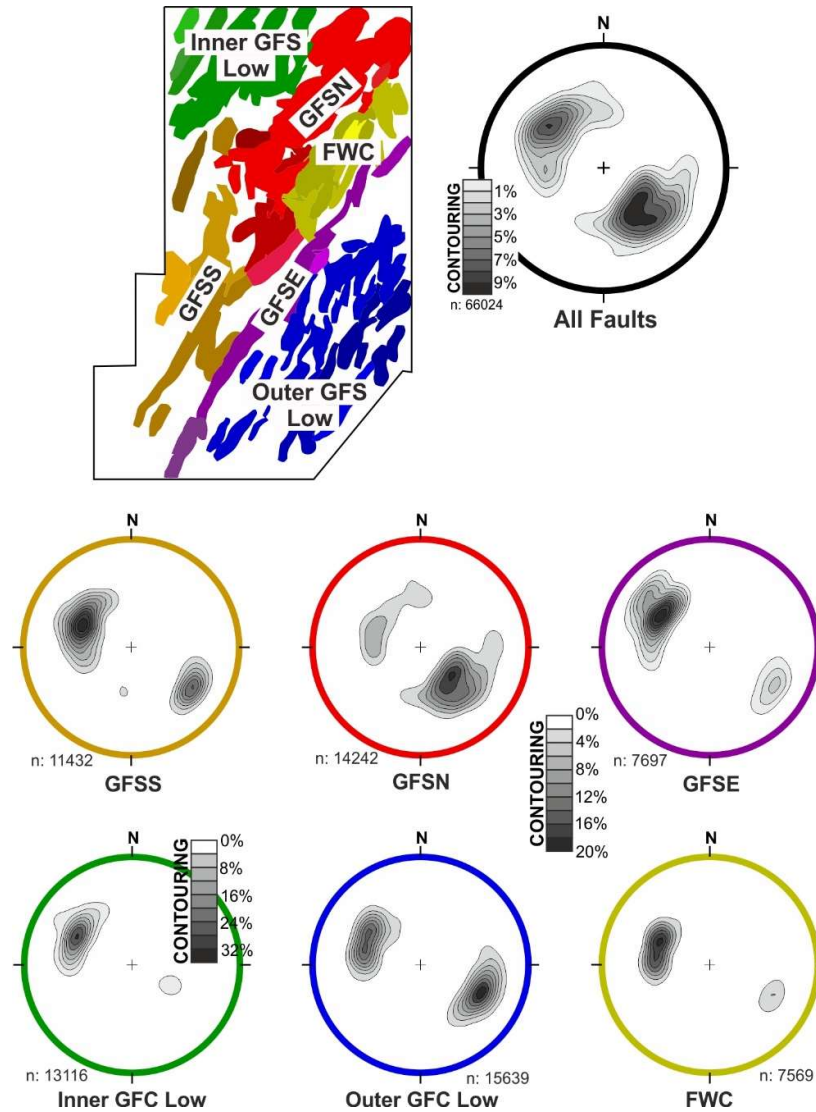

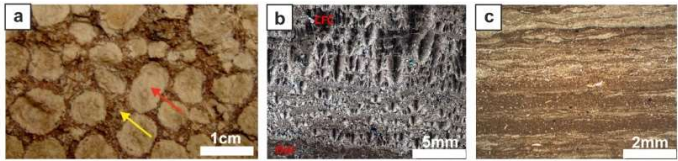


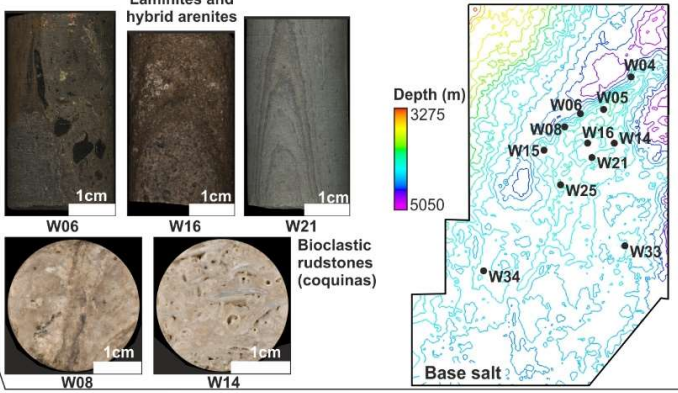


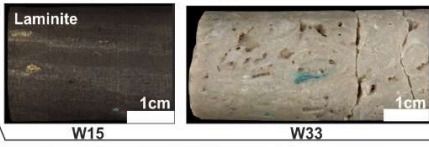

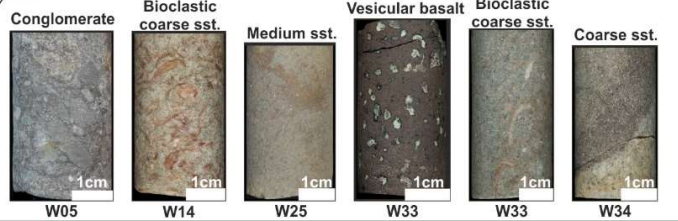



Figure A4: Map view of the structural compartments on which the faults are coloured accordingly to the respective stereographic projections. The stereographic projection for all the faults is also shown. Notice that the fault segments of the GFS branches are NE-SW oriented, while the faults elsewhere, in the low strain compartments, are predominantly NNE-SSW oriented.

TECTONIC/ DEP.STAGE	UNCONF.	LITHOTYPES	LITHOTYPES DESCRIPTION
Salt	 SBU		a) Core photograph of calcite pisoids (red arrow) replacing stevensite further replaced by dolomite (yellow arrow) (from Herlinger et al., 2017). b) Thin section (cross-polarised light) of fascicular-optic calcite crusts (CFC) intercalated with granular deposits replaced by dolomite (Dol) (from Lima & De Ros, 2019). c) Planar to wavy laminite with millimetric laminations defined by the predominance of clay and microcrystalline dolomite (uncrossed polarised) (from Lima & De Ros, 2019).
Post-rift II (PRII)	 IPRU		
Post-rift I (PRI)			
	 PRU		
Rift transition (RTR)			Bioclastic rudstones and grainstones are constituted of bivalve bioclasts, ooids, and peloids. The bioclasts occur in a range of grain sizes, from coarse sand to pebble, and the fragmented shells often constitute the finer fraction. Diagenetic alteration is commonly represented by dolomite, calcite, and quartz replacing bioclasts and as intergranular cement.
Syn-rift III (SRIII)	 tRift		Laminites and hybrid arenites are constituted of detrital quartz, micas, ostracoids and peloid bioclasts at (most commonly) fine sand grain size, in a siliciclastic muddy matrix; zircon is a common detrital accessory. Diagenetic nodules of calcite or dolomite, partially replaced by microcrystalline quartz and pyrite are common.
Syn-rift II (SRII)	 tSRII		For a detailed facies and facies association description of the equivalent to SRIII and RTR TSSs, see Olivito & Souza (2020).
	 tl/A		
Syn-rift I (SRI) (Rift initiation)			The conglomerates are constituted of angular clasts of basement and basalt with intense carbonate (mostly dolomite) cementation and replacement. The sandstones are made of arkoses with angular, poorly sorted clasts of feldspar, quartz and muscovite (and accessory zircon), whose grain sizes ranges from fine sand to granule. Most common cementation is made by dolomite and ferroan dolomite.
	 tBas		
BASEMENT			

(caption on next page)

Figure A5: Side-wall cores and thin sections representing the main lithofacies for each of the TSS (see text for description). There is no wellbore data for the SRII. A structural map of the bSalt horizon with the location of the wells from whose samples are described is also shown.

REFERENCES (FOR ANNEXES)

- Cowie, P. (1998). A healing–reloading feedback control on the growth rate of seismogenic faults. *Journal of Structural Geology*, 20, 1075-1087. [https://doi.org/10.1016/S0191-8141\(98\)00034-0](https://doi.org/10.1016/S0191-8141(98)00034-0)
- Herlinger Jr., R., Zambonato, E.E. & De Ros, L.F. (2017). Influence of Diagenesis On the Quality of Lower Cretaceous Pre-salt Lacustrine Carbonate Reservoirs from Northern Campos Basin, Offshore Brazil. *Journal of Sedimentary Research*, 87, 1285-1313. <https://doi.org/10.2110/jsr.2017.70>
- Kim, Y.-S. & Sanderson, D.J. (2005). The relationship between displacement and length of faults: a review. *Earth Science Reviews*, 68, 317-334. <https://doi.org/10.1016/j.earscirev.2004.06.003>
- Lima, B.E.M. & De Ros, L.F. (2019). Deposition, diagenetic and hydrothermal processes in the Aptian Pre-Salt lacustrine carbonate reservoirs of the northern Campos Basin, offshore Brazil. *Sedimentary Geology*, 383, 55-81. <https://doi.org/10.1016/j.sedgeo.2019.01.006>
- McLeod, A.E., Dawers, N.H. & Underhill, J.R. (2000). The propagation and linkage of normal faults: insights from the Strathspey–Brent–Statfjord fault array, northern North Sea. *Basin Research*, 12, 263-284. <https://doi.org/10.1111/j.1365-2117.2000.00124.x>
- Morley, C.K. (2017). The impact of multiple extension events, stress rotation and inherited fabrics on normal fault geometries and evolution in the Cenozoic rift basins of Thailand. *Geological Society, London, Special Publications*, 439, 413-445. <https://doi.org/10.1144/SP439.3>
- Olivito, J.P.R. & Souza, F.J. (2020). Depositional model of early Cretaceous lacustrine carbonate reservoirs of the Coqueiros formation-Northern Campos Basin, southeastern Brazil. *Marine and Petroleum Geology*, 111, 414-439. <https://doi.org/10.1016/j.marpetgeo.2019.07.013>
- Rotevatn, A., Jackson, C.A.-L., Tvedt, A.B., Bell, R.E. & Blækkan, I. (2019). How do normal faults grow? *Journal of Structural Geology*, 125, 174-184. <https://doi.org/10.1016/j.jsg.2018.08.005>
- Schlagenhauf, A., Manighetti, I., Malavieille, J. & Dominguez, S. (2008). Incremental growth of normal faults: Insights from a laser-equipped analog experiment. *Earth and Planetary Science Letters*, 273, 299-311. <https://doi.org/10.1016/j.epsl.2008.06.042>
- Schlische, R.W., Young, S.S., Ackermann, R.V. & Gupta, A. (1996). Geometry and scaling relations of a population of very small rift-related normal faults. *Geology*, 24, 683-686. [https://doi.org/10.1130/0091-7613\(1996\)024%3C0683:GASROA%3E2.3.CO;2](https://doi.org/10.1130/0091-7613(1996)024%3C0683:GASROA%3E2.3.CO;2)
- Schultz, R.A., Soliva, R., Fossen, H., Okubo, C.H. & Reeves, D.M. (2008). Dependence of displacement–length scaling relations for fractures and deformation bands on the volumetric changes across them. *Journal of Structural Geology*, 30, 1405-1411. <https://doi.org/10.1016/j.jsg.2008.08.001>